Nanoscale

PAPER

View Article Online
View Journal | View Issue

Cite this: *Nanoscale*, 2024, **16**, 16998

Multi-functional $GdEu_xTb_{1-x}O_3$ (x = 0 to 1) nanoparticles: colour tuning optical properties, water proton spin relaxivities, and X-ray attenuation properties†

Dejun Zhao, [a] Ying Liu,[a] Son Long Ho, [a] Tirusew Tegafaw,[a] Abdullah Khamis Ali Al Saidi, [a] Hansol Lee,[b] Dabin Ahn,[b] Hyunji Nam,[b] Ji Ae Park,[c] Ji-ung Yang,[c] Weon-Sik Chae, [d] Yongmin Chang*[e] and Gang Ho Lee *[a]

Received 23rd May 2024,
Accepted 21st August 2024

DOI: 10.1039/d4nr02195a

rsc.li/nanoscale

Multi-functional nanoparticles are useful for various applications, such as biomedical imaging, detection, and display technologies. Colour-tunable $GdEu_xTb_{1-x}O_3$ nanoparticles were synthesized with emission colour ranging from green (545 nm) to red (616 nm) by varying x (x = 0, 0.1, 0.3, 0.5, 0.7, 0.9, and 1). These nanoparticles were surface-grafted with polyacrylic acid and a small quantity of 2,6-pyridinedicarboxylic acid. This modification aimed to ensure long-term colloidal stability (>1 year without precipitation) and high quantum yields (>30%) in aqueous media. Additionally, they exhibited long emission lifetimes (~1 ms), high longitudinal water proton spin relaxivities (>30 $s^{-1}mM^{-1}$), and high X-ray attenuation efficiencies (~10 HU mM^{-1}). These multiple exceptional properties within a single nanoparticle make them highly valuable for applications in biomedical imaging, noise-free signal detection, and colour display.

Introduction

The mixed lanthanide oxide ($GdEu_xTb_{1-x}O_3$) nanoparticles exhibit various optical and magnetic properties essential for applications in biology, medicine, and information technology, including biolabeling, diagnosis, and electronic displays.[1–5] These properties stem from the intrinsic electronic properties of 4f-electrons of the lanthanide elements,[6] and their high atomic numbers, which enhance their X-ray attenuation power.[7]

In this study, gadolinium (Gd), europium (Eu), and terbium (Tb) were mixed to obtain $GdEu_xTb_{1-x}O_3$ nanoparticles, with Gd maintained at a nearly constant level to adjust the emission colour between green (545 nm from Tb) and red (616 nm from Eu)[1,2,8] by varying x (x = 0–1). Gd^{3+} is optically transparent in the visible region and has no effect on the colour.[9] However, it significantly boosts longitudinal water proton spin relaxivities (r_1) due to its exceptionally high 4f-electron spin (s = 7/2) magnetic moment (μ = 7.9–8.0 emu g^{-1}), valuable for use as T_1 magnetic resonance imaging (MRI) contrast agents.[4,5,10–12]

Lanthanides, as optical probes, exhibit exceptional properties such as long-term photostability, a large Stokes shift (the energy difference between excitation and emission wavelengths), sharp atomic-like transitions, long emission lifetimes, and resistance to photobleaching.[1,5,13,14] Consequently, they enable near background-free signal measurements with high detection limits,[15] surpassing organic dyes and quantum dots (QDs). However, their drawback is low emission intensity due to forbidden 4f–4f electronic transitions,[1,16,17] making them less favoured as optical probes than organic dyes and QDs. Nevertheless, this can be significantly improved through photosensitization,[8,18–25] which is an electronic energy transfer process from organic chromophores to lanthanides. The photosensitized lanthanide materials in aqueous media emit strongly with high quantum yields (QYs),[8,22,23] comparable to or even surpassing those[26] of organic dyes.

Photosensitized $GdEu_xTb_{1-x}O_3$ nanoparticles were created in this study, embodying multiple-functionalities within a

[a]*Department of Chemistry, College of Natural Sciences, Kyungpook National University, Taegu 41566, South Korea. E-mail: ghlee@mail.knu.ac.kr; Fax: +82-53-950-6330; Tel: +82-53-950-5340*
[b]*Department of Medical & Biological Engineering, Kyungpook National University, Taegu 41944, South Korea*
[c]*Division of RI-Convergence Research, Korea Institute of Radiological & Medical Science, Seoul 01817, South Korea*
[d]*Daegu Center, Korea Basic Science Institute, Taegu 41566, South Korea*
[e]*Department of Molecular Medicine, School of Medicine, Kyungpook National University, Taegu 41944, South Korea. E-mail: ychang@knu.ac.kr; Tel: +82-53-420-5471*

†Electronic supplementary information (ESI) available: EDS spectra, laser light scattering images, XRD patterns and analyzed data, excitation spectra, UV-visible absorption spectrum, FT-IR absorption peak assignments, CIE (1931) chromaticity coordinates, and PL peak assignments. See DOI: **https://doi.org/10.1039/d4nr02195a**

single nanoparticle. Until now, achieving colour tuning using Eu and Tb required varying doping ratios of Eu^{3+}/Tb^{3+} ions in various nano to micro solid-state matrices[27–32] or mixing Eu^{3+}/Tb^{3+} complexes in different ratios.[33–36] In this study, colour-tunable $GdEu_xTb_{1-x}O_3$ nanoparticles with multiple properties within a single nanoparticle, useful for various applications in solid-states and colloidal forms in aqueous media, were synthesized for the first time. After being grafted with hydrophilic and biocompatible polyacrylic acid (PAA) and a small amount of the organic photosensitizer 2,6-pyridinedicarboxylic acid (PDA), the $GdEu_xTb_{1-x}O_3$@PAA/PDA nanoparticle colloids maintained stability in aqueous media without precipitation after synthesis for >1 year, while emitting photons with high QYs. Photoluminescent (PL) spectra, colour tuning, absolute QYs, emission lifetimes, water proton spin relaxivities, and X-ray attenuation power of the nanoparticles were measured to unveil their multi-functional properties. Their key properties include colour tunability by varying x with high QYs, suitable for colour display applications; long emission lifetimes, beneficial for noise-free signal detection; and multiple imaging properties, useful for optical imaging, T_1 MRI, and X-ray computed tomography (CT).

Experimental

Materials

Gadolinium(III) chloride hexahydrate ($GdCl_3{\cdot}6H_2O$, ≥99%), europium(III) chloride hexahydrate ($EuCl_3{\cdot}6H_2O$, ≥99.9%), terbium(III) chloride hexahydrate ($TbCl_3{\cdot}6H_2O$, ≥99.9%), PAA (M_w = ~1800 amu), PDA ($C_7H_5NO_4$, ≥98.0%), dimethyl sulfoxide (C_2H_6OS, DMSO, ≥99.9%), tetramethylammonium hydroxide solution ($C_4H_{13}NO$, TMAH, 25 wt% in methanol), and dialysis tubes [molecular weight cut-off (MWCO) = 500 and 2000 amu] were purchased from Sigma-Aldrich (USA). Ethanol (C_2H_5OH, ≥99.0%) and sodium hydroxide (NaOH, >99%) were purchased from Duksan (South Korea). All chemicals were used as received. The synthesized nanoparticles were washed and dispersed using triple-distilled water.

Synthesis of $GdEu_xTb_{1-x}O_3$@PAA nanoparticles

Fig. 1a schematically shows that 1 mmol $GdCl_3{\cdot}6H_2O$, x mmol $EuCl_3{\cdot}6H_2O$, and $(1-x)$ mmol $TbCl_3{\cdot}6H_2O$ (x = 0.1, 0.3, 0.5, 0.7, and 0.9) were dissolved in 15 mL DMSO with magnetic stirring in a three-necked round-bottom flask at 35 °C under atmospheric conditions. For x = 0 and 1, 1 mmol $GdCl_3{\cdot}6H_2O$ and 0.3 mmol $LnCl_3{\cdot}6H_2O$ (Ln = Eu or Tb) were used. After all precursors were dissolved, the solution became transparent. Subsequently, TMAH solution was added to maintain the solution pH at ~8, followed by 24 h of magnetic stirring to yield mixed lanthanide oxide nanoparticles. In a separate beaker, 1 mmol of PAA was dissolved in 10 mL of DMSO under magnetic stirring to prepare the PAA solution. This solution was subsequently added to the nanoparticle solution, and TMAH solution was added to maintain the solution pH at ~8. After 24 h of magnetic stirring, PAA-grafted nanoparticles were obtained. Ethanol (200 mL) was added to the solution, followed by centrifugation at 4000 rpm to purify PAA-grafted nanoparticles. This step removed top solutions containing DMSO, unreacted lanthanide precursors, TMAH, and PAA. After three repetitions of the washing process, the nanoparticles were dispersed in triple-distilled water. Subsequently, a 1 M NaOH solution prepared in triple-distilled water was added to adjust the solution pH to ~8. The nanoparticles underwent further purification through 1 day of dialysis (MWCO = 2000 amu).

PDA grafting to obtain $GdEu_xTb_{1-x}O_3$@PAA/PDA nanoparticles

The PDA grafting is schematically shown in Fig. 1b. PDA solutions at concentrations of 10, 20, 30, 40, and 50 μM were prepared in triple-distilled water. These solutions were then added to 4 mL of the prepared $GdEu_xTb_{1-x}O_3$@PAA nanoparticle solutions ([Eu] + [Tb] = 2 mM), and the mixtures were gently shaken for 1 min to yield $GdEu_xTb_{1-x}O_3$@PAA/PDA nanoparticles. The solutions underwent 1 day of dialysis (MWCO = 500 amu) to remove excess PDA. The optimal PDA concentration was determined by analyzing PL spectra to achieve the highest PL intensity.

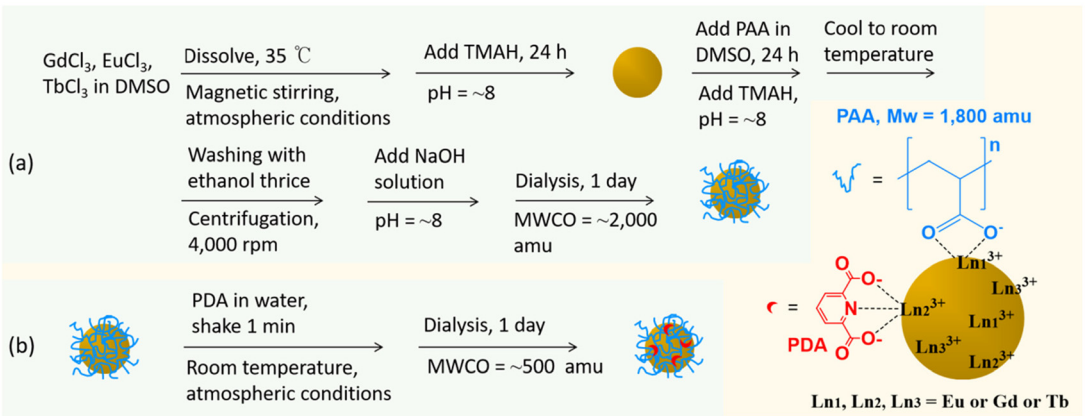

Fig. 1 Syntheses of (a) $GdEu_xTb_{1-x}O_3$@PAA nanoparticles and (b) $GdEu_xTb_{1-x}O_3$@PAA/PDA nanoparticles (x = 0, 0.1, 0.3, 0.5, 0.7, 0.9, and 1).

Characterizations

The synthesized nanoparticles underwent various analyses, as previously detailed.[8] These characterizations included particle diameter measurements using high-resolution transmission electron microscopy (HRTEM), metal composition determination using energy-dispersive X-ray spectroscopy (EDS), crystal structure analysis using X-ray diffraction (XRD), zeta

Table 1 Physicochemical properties of $GdEu_xTb_{1-x}O_3$@PAA/PDA nanoparticles

	ICP-AES (atomic %)			EDS (atomic %)							
x	Gd	Eu	Tb	Gd	Eu	Tb	d_{avg} (nm)	ζ (mV)	S^a (wt%)	δ^b (nm^{-2})	N_{PAA} ^{c}
0	72.7	0	27.3	56.5	0	43.5	1.8	−27.3	67.3 (28.1)	1.8	18
0.1	51.6	5.3	43.1	47.0	6.2	46.8	2.0	−21.9	62.8 (30.4)	1.7	22
0.3	51.2	16.0	32.8	48.2	14.8	37.0	2.0	−32.9	62.1 (26.3)	2.0	25
0.5	50.4	26.6	23.0	47.9	23.6	28.5	2.2	−23.4	63.3 (27.9)	2.1	31
0.7	50.0	36.5	13.5	48.0	33.3	18.7	2.0	−26.9	63.9 (28.8)	1.8	23
0.9	49.4	46.3	4.3	48.3	43.1	8.6	2.3	−34.7	60.4 (27.9)	2.0	34
1	68.0	32.0	0	77.7	22.3	0	2.0	−26.9	69.1 (27.5)	2.0	26

^{a} Surface-grafting wt% of PAA and PDA, with values in parentheses indicating the wt% relative to $GdEu_xTb_{1-x}O_3$ nanoparticles. ^{b} Surface-grafting density,[49] representing the average number of PAA polymers covering a nanoparticle unit surface area. ^{c} Average number of PAA polymers covering a nanoparticle surface ($= \delta \times \pi d_{avg}^2$).

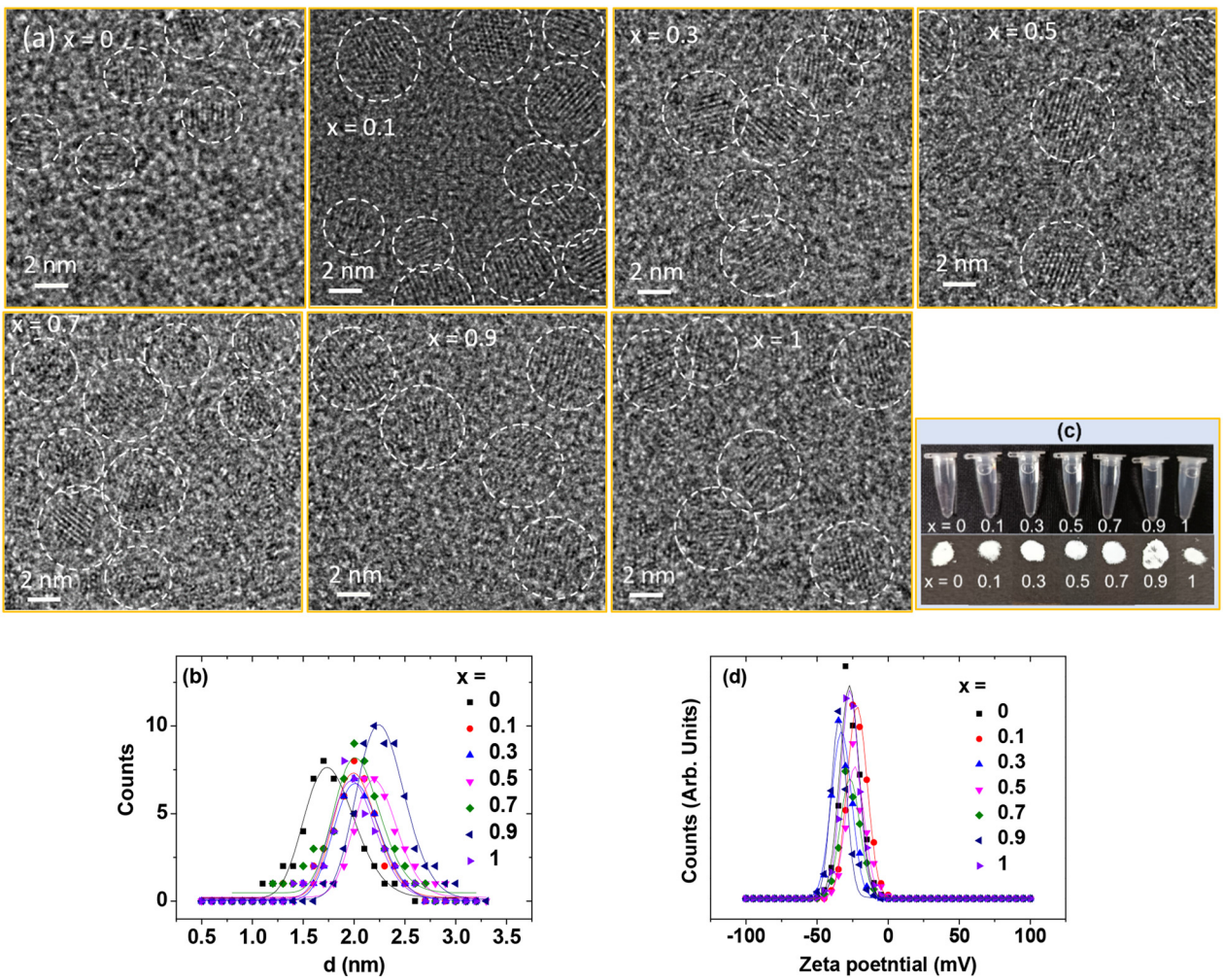

Fig. 2 $GdEu_xTb_{1-x}O_3$@PAA/PDA nanoparticles (x = 0, 0.1, 0.3, 0.5, 0.7, 0.9, and 1): (a) HRTEM images, (b) log–normal function fits depicting the observed particle diameter distributions, (c) images of solution samples (top), showing good colloidal stability in aqueous media, and powder samples (bottom), and (d) zeta potential curves and Gaussian function fits.

potential measurements using a zeta size analyzer, metal composition determination and metal concentration analysis in aqueous media using inductively coupled plasma-atomic emission spectroscopy (ICP-AES), surface-grafting assessment of PAA and PDA on nanoparticle surfaces using Fourier-transform infrared (FT-IR) absorption spectroscopy, surface-grafting quantity determination of PAA and PDA using thermogravimetric analysis (TGA), Ultraviolet (UV)-visible absorption, PL, and excitation spectra, and fluorescence lifetimes measured with a PL spectrometer, absolute QYs assessed using an integration sphere in a PL spectrometer, phantom images and X-ray attenuation power measured using a CT scanner, water proton spin relaxivities and map images acquired using a 3 T MRI scanner at 22 °C, and evaluation of cellular cytotoxicity on two cell lines purchased from American Type Culture Collection (Manassas, VA, USA): normal alpha mouse liver 12 (AML12) and immortalized human embryonic kidney (Hek293) cells using the 3-(4,5-dimethylthiazol-2-yl)-2,5-diphenyl-2*H*-tetrazolium bromide (MTT) assay.

Results and discussion

Colloidal stability, particle diameter, zeta potential, and crystal structure

The $GdEu_xTb_{1-x}O_3$@PAA/PDA nanoparticles were labelled as x = 0, 0.1, 0.3, 0.5, 0.7, 0.9, and 1, representing the mole compositions used in the synthesis. The actual compositions (x) were estimated from ICP-AES and EDS analyses (Table 1). The EDS spectra are provided in Fig. S1 (ESI†), confirming the presence of Eu, Gd, and Tb in the nanoparticles. As illustrated in the HRTEM images (Fig. 2a), the particle diameters of the nanoparticles were ultrasmall, ranging from 1 to 3 nm. The average particle diameters (d_{avg}s) were estimated at 1.8, 2.0, 2.0, 2.2, 2.0, 2.3, and 2.0 nm for x = 0, 0.1, 0.3, 0.5, 0.7, 0.9, and 1, respectively, using log–normal function fits (Fig. 2b & Table 1). Fig. 2c presents the nanoparticle solution and powder sample images. The solution samples remained transparent without nanoparticle precipitation after synthesis (>1 year), demonstrating strong colloidal stability in aqueous media due to the hydrophilic PAA polymer grafting on the nanoparticle surfaces. Despite the photosensitizer PDA, having low water solubility,[37] its minor amount during synthesis did not affect colloidal stability. The colloidal dispersion of the nanoparticles in aqueous media was confirmed through laser light scattering, known as the Tyndall effect (Fig. S2 in ESI†). The high negative zeta potentials ($\zeta < -20$ mV) were observed (Fig. 2d & Table 1), confirming their good colloidal stability in aqueous media.

Eu^{3+}, Tb^{3+}, and Gd^{3+} can be homogeneously mixed within mixed lanthanide oxide nanoparticles due to their identical cubic crystal structure[38–42] and similar ionic radii.[43] The nanoparticles exhibited an amorphous pattern due to their ultrasmall particle diameters (Fig. S3a in ESI†). However, distinct sharp peaks indicative of the cubic structure were observed after TGA owing to the heat treatment[44] (Fig. S3b in ESI†). The lattice constants after TGA were consistent with mole-percent averaged values of those of individual bulk Ln_2O_3 (Ln = Eu, Gd, and Tb)[38–40] (Table S1 in ESI†), confirming the homogeneous mixing of the different Ln^{3+} within the nanoparticles.

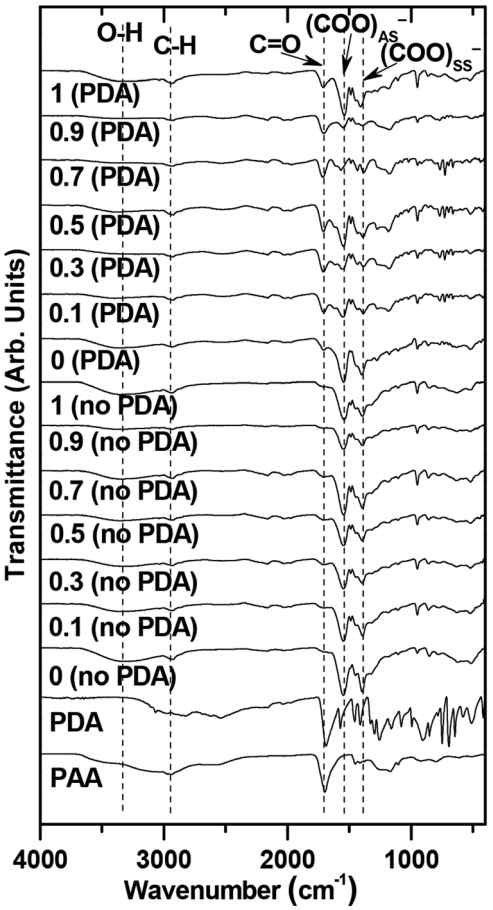

Fig. 3 FT-IR absorption spectra of PAA, PDA, $GdEu_xTb_{1-x}O_3$@PAA nanoparticles (labelled as "no PDA"), and $GdEu_xTb_{1-x}O_3$@PAA/PDA nanoparticles (labelled as "PDA") (x = 0, 0.1, 0.3, 0.5, 0.7, 0.9, and 1). Subscripts "AS" and "SS" indicate asymmetric and symmetric stretchings, respectively.

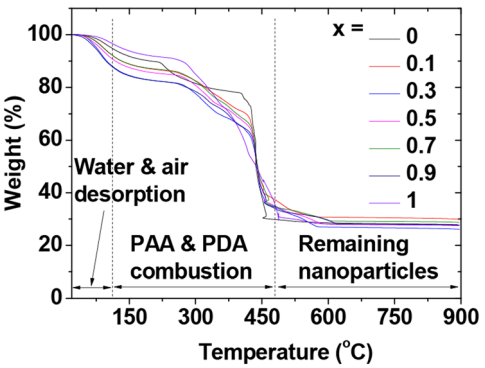

Fig. 4 TGA curves of $GdEu_xTb_{1-x}O_3$@PAA/PDA nanoparticles (x = 0, 0.1, 0.3, 0.5, 0.7, 0.9, and 1) under air flow.

Surface grafting of PAA and PDA on the nanoparticle surfaces

PAA and PDA are grafted on the nanoparticle surfaces through electrostatic interaction between their –COOH groups and the Ln^{3+} ions of the nanoparticles. In addition, the nitrogen of PDA can contribute to the interaction. The binding structure of PAA and PDA is proposed in Fig. 1. Multiple binding between each PAA and a nanoparticle is possible because of ~27 –COOH groups per PAA and numerous Ln^{3+} ions on each nanoparticle surface. The FT-IR absorption spectra of $GdEu_xTb_{1-x}O_3$@PAA/PDA nanoparticles (x = 0, 0.1, 0.3, 0.5, 0.7, 0.9, and 1), and their references, including $GdEu_xTb_{1-x}O_3$@PAA nanoparticles, PAA, and PDA, are presented in Fig. 3. Before binding to the nanoparticles, the C=O stretching peak of PAA at ~1700 cm^{-1} red-shifted and split into COO^- antisymmetric stretching vibrations at ~1548 cm^{-1} and symmetric stretching vibrations at ~1396 cm^{-1} after binding to the nanoparticles[45,46] (Fig. 3). This shift and splitting indicate bidentate[47] electrostatic (*i.e.*, hard acid-base[48]) binding of COO^- groups of PAA to the Ln^{3+} of the nanoparticles. The C=O stretching peak intensity at ~1700 cm^{-1} increased after PDA binding to the nanoparticles compared to that before binding (Fig. 3), confirming the successful electrostatic binding of COO^- groups of PDA to the Ln^{3+} of the nanoparticles. Key absorption peak frequencies, supporting the successful PAA and PDA grafting on the nanoparticles, are provided in Table S2.†

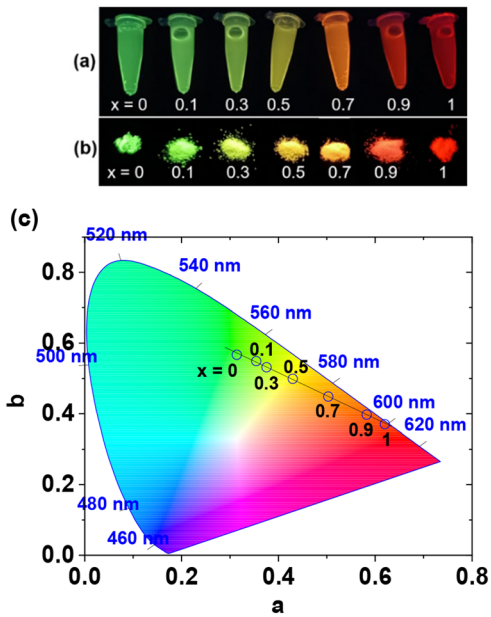

Fig. 5 Images of (a) aqueous solution samples and (b) powder samples of $GdEu_xTb_{1-x}O_3$@PAA/PDA nanoparticles (x = 0, 0.1, 0.3, 0.5, 0.7, 0.9, and 1) under 254 nm UV irradiation, illustrating the colour tuning between green and red by adjusting x. (c) CIE (1931) chromaticity system, showing the colour tuning between green and red.

Surface-grafting amount of PAA

The major grafting ligand on the nanoparticle surfaces was PAA, given its larger quantity (1 mmol) compared to PDA (10–50 μmol) used during synthesis. Surface-grafting amounts (S) were determined in wt% from TGA curves. Fig. 4 illustrates mass drops due to water and air desorption between room temperature and ~110 °C. Afterward, PAA and PDA were removed from the nanoparticles at temperatures up to ~410 °C due to a combustion reaction with flowing hot air. Estimated grafting amounts for PAA and PDA were ~63% (Table 1), after accounting for water and air desorption. Then, TGA curves remained flat, indicating remaining mixed lanthanide oxide nanoparticles with a wt.% of ~28% (Table 1), as confirmed by the crystalline XRD patterns after TGA (Fig. S3 in ESI†). The average number of PAA polymers grafting a nanoparticle unit surface area, *i.e.*, surface-grafting densities (δ),[49] and the average number (N_{PAA}) of PAA polymers grafting a nanoparticle surface were estimated to be ~1.9 nm^{-2} and ~25, respectively (Table 1). These estimates relied on the above-estimated surface-grafting wt% of PAA polymers (excluding minor PDA surface-grafting wt%), d_{avg}s obtained from HRTEM images, and mole% averaged bulk densities[50] of different Ln_2O_3 (Ln = Eu, Gd, and Tb).

Optical properties: colour tuning, excitation and PL spectra, absolute QYs, and emission lifetimes

Colour tuning. The lanthanide ion concentrations used for all optical property measurements are provided in Table S3.†

Table 2 Optical (λ_{ex}, absolute QY, and τ) properties, water proton spin relaxivities (r_1 and r_2), and X-ray attenuation efficiency (η) of $GdEu_xTb_{1-x}O_3$@PAA/PDA nanoparticles in aqueous media (x = 0, 0.1, 0.3, 0.5, 0.7, 0.9, and 1)

		Absolute QY (%)		τ (ms)		r_1[a] (s^{-1} mM^{-1})		r_2[a] (s^{-1} mM^{-1})		η[a] (HU mM^{-1})		
x	λ_{ex} (nm)	No PDA	PDA	616 nm peak (Eu)	545 nm peak (Tb)	No. PDA	PDA	No. PDA	PDA	35 kVp	50 kVp	75 kVp
0	290	7.9	35.8	—	1.850	—	—	—	—	12.0	10.0	9.7
0.1	289	5.8	36.2	1.113	1.447	43.4	31.3	95.7	58.6	—	—	—
0.3	289	7.3	34.1	0.700	1.222	45.2	26.1	88.0	48.4	—	—	—
0.5	287	3.8	39.7	0.910	1.369	49.0	34.7	88.0	63.8	—	—	—
0.7	289	2.5	31.2	0.843	1.361	—	—	—	—	—	—	—
0.9	288	2.3	20.0	0.811	1.429	60.8	38.2	95.6	70.6	—	—	—
1	288	6.9	51.6	0.413	—	—	—	—	—	10.8	9.0	9.1

[a] For r_1, r_2, and η, total concentration of (Eu + Gd + Tb) was used.

Eu and Tb emit red (616 nm) and green (545 nm) light,[1,2,8] respectively, while Gd is optically transparent in the visible range.[9] Fig. 5a & b show $GdEu_xTb_{1-x}O_3$@PAA/PDA nanoparticle solution and powder sample images under 254 nm UV light irradiation, demonstrating colour tuning between green and red with strong emission intensity by varying x from 0 to 1. Additionally, the colour tunability is displayed in the Commission International de l'Eclairagein (CIE) (1931) system[29,31,36] (Fig. 5c) with CIE chromaticity coordinates (a,b) for all values of x listed in Table S4 (ESI†). The approximate colour corresponding to each CIE coordinate (a,b) in Fig. 5c is provided in Table S4.† Fig. 5c shows that the CIE coordinates (a,b) align with previous studies,[29,36] and CIE coordinate 'b' varies linearly with 'a' as $b = 0.77715–0.65297a$, consistent with the findings of Qin and Tang.[31] The CIE coordinates for reddish orange ($x = 1$; $a = 0.6197$, $b = 0.3706$) and yellowish green ($x = 0$; $a = 0.3141$, $b = 0.5674$) of the nanoparticles closely match the red (0.67, 0.33) and green (0.21, 0.71) coordinates of the National Television Standard Committee (NTSC),[51] suggesting the suitability of the nanoparticles for colour display applications. Although not studied here, the $GdEu_xTb_{1-x}O_3$@PAA/PDA nanoparticles may also emit visible photons under X-ray irradiation,[52–54] valuable for use as X-ray scintillators in X-ray imaging.

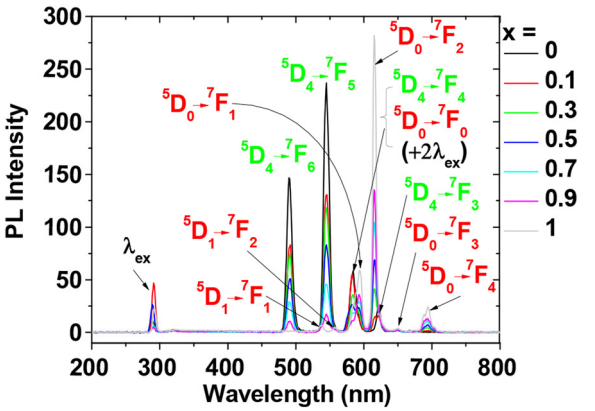

Fig. 6 PL spectra of $GdEu_xTb_{1-x}O_3$@PAA/PDA nanoparticles in aqueous media (x = 0, 0.1, 0.3, 0.5, 0.7, 0.9, and 1) obtained using λ_{ex}s (Table 2).

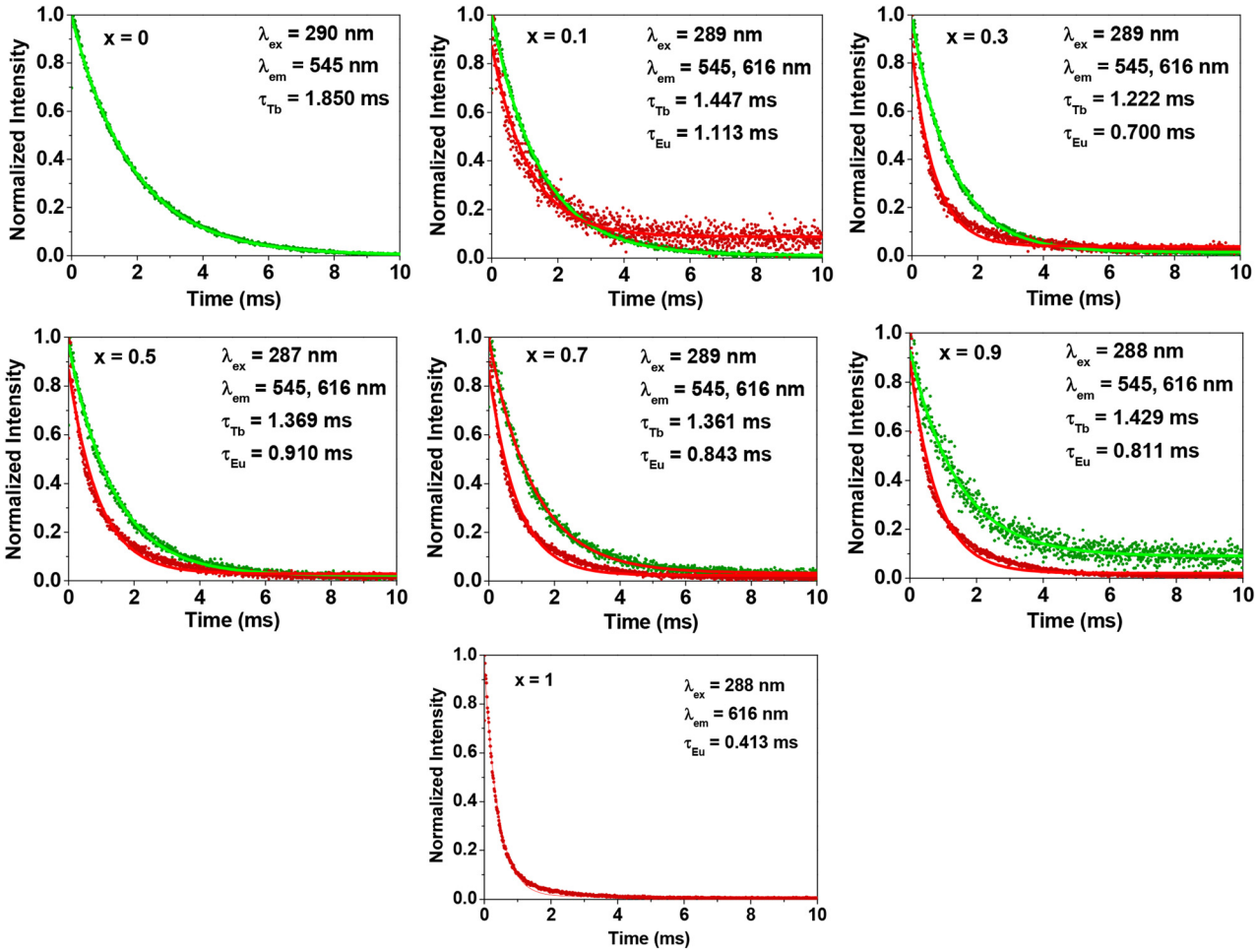

Fig. 7 TRF spectra of $GdEu_xTb_{1-x}O_3$@PAA/PDA nanoparticles in aqueous media (x = 0, 0.1, 0.3, 0.5, 0.7, 0.9, and 1). The λ_{ex}, λ_{em}, and τ_{Ln} (Ln = Eu or Tb) indicate excitation wavelength, emission wavelength, and photoemission lifetime, respectively. The intensity was normalized relative to that at time = 0.

Excitation spectra

To determine the excitation wavelengths (λ_{ex}) for taking PL spectra, excitation spectra of $GdEu_xTb_{1-x}O_3$@PAA/PDA nanoparticles in aqueous media (Fig. S4†) were measured using the most intense emission peaks of Tb at 545 nm and Eu at 616 nm as references. The resulting λ_{ex} values are provided in Table 2. These λ_{ex} values closely match the strong absorption peaks of PDA at ~275 nm in its pure and conjugated nanoparticle (x = 0, 1) UV-visible absorption spectra (Fig. S5†). This similarity indicates that PDA, acting as a photosensitizer, efficiently absorbs photons at 260–295 nm and transfers energy to the $GdEu_xTb_{1-x}O_3$@PAA/PDA nanoparticles.

PL spectra

The PL spectra of $GdEu_xTb_{1-x}O_3$@PAA/PDA nanoparticles in aqueous media showed strong emission from Eu^{3+} and Tb^{3+} at the determined λ_{ex}s (Fig. 6). The transition wavelengths and assignments are detailed in Table S5 (ESI†). The peaks exhibited sharp, atomic-like transitions [full widths at half maximum (FWHM) = ~10 nm] and significant Stokes shifts (>200 nm). These exceptional optical properties contrast with organic dyes with typically broad emission peaks and smaller Stokes shifts (<50 nm). Similarly, QDs exhibit somewhat narrow peak FWHMs (~20 nm) but smaller Stokes shifts (<50 nm).[55]

Absolute QYs

The absolute QYs measured in aqueous media are presented in Table 2. These values are 7 to 10 times higher than those without PDA (Table 2), demonstrating the crucial role of photosensitization for the lanthanides. These QY values are comparable to or higher than those of organic dyes.[26]

Photoemission lifetimes and energy transfer efficiencies

The photoemission lifetimes (τ_s) of $GdEu_xTb_{1-x}O_3$@PAA/PDA nanoparticles in aqueous media were estimated from time-resolved fluorescence (TRF) spectra and by fitting the spectra

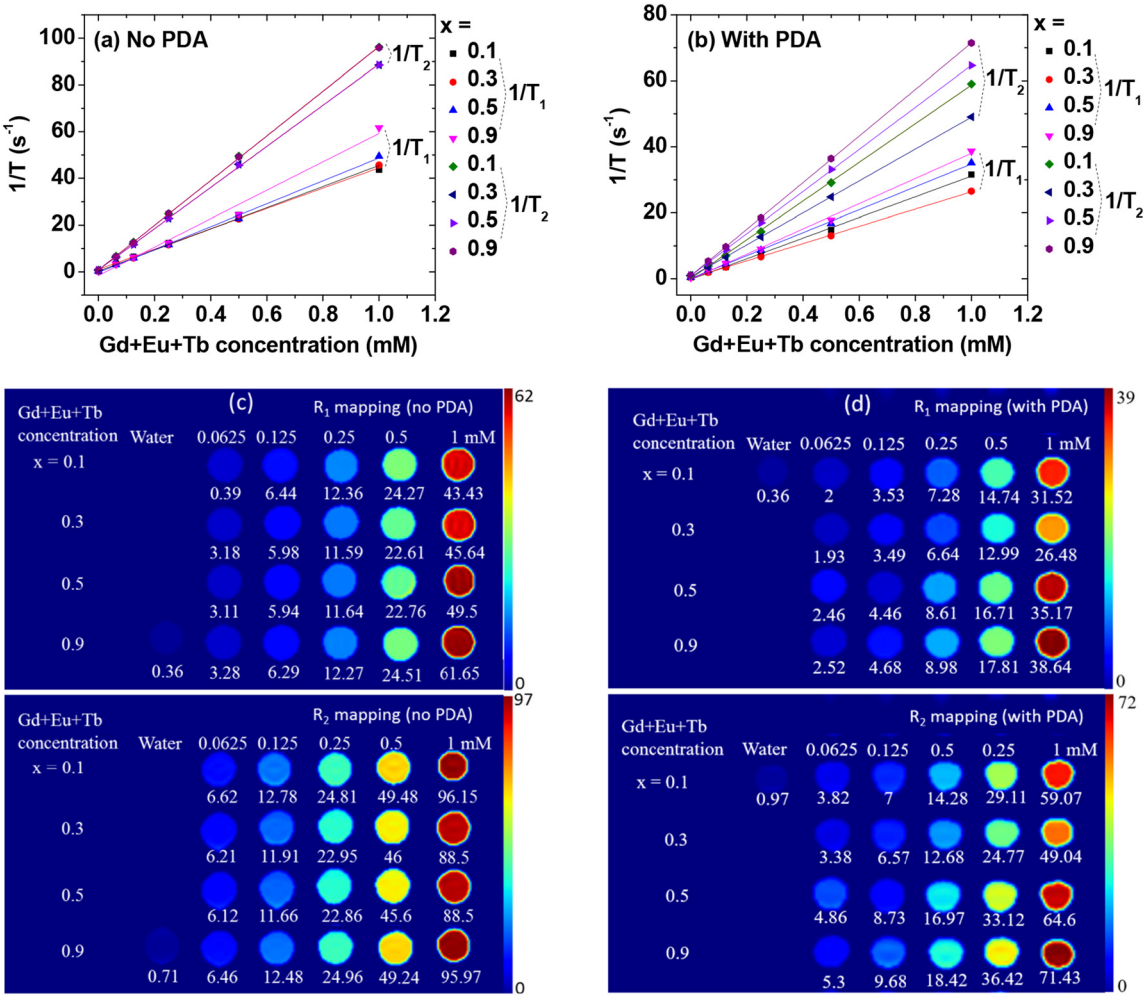

Fig. 8 Plots of $1/T_1$ and $1/T_2$ against concentrations (mM) of Eu + Gd + Tb for (a) $GdEu_xTb_{1-x}O_3$@PAA nanoparticles and (b) $GdEu_xTb_{1-x}O_3$@PAA/PDA nanoparticles in aqueous media (x = 0.1, 0.3, 0.5, and 0.9). The slopes represent r_1 and r_2 values, respectively. R_1 and R_2 maps with varying Eu + Gd + Tb concentrations (mM) for (c) $GdEu_xTb_{1-x}O_3$@PAA nanoparticles and (d) $GdEu_xTb_{1-x}O_3$@PAA/PDA nanoparticles in aqueous media. The values below the maps indicate $1/T_1$ (= R_1) and $1/T_2$ (= R_2) values (s^{-1}).

to an exponential decay function (Fig. 7). The obtained τ values were ~1 ms (Table 2), significantly 10^5 to 10^6 times longer than those of organic dyes (~10^{-9} s)[56,57] and QDs (~10^{-8} s).[56,58] These longer emission lifetimes are highly valuable as they enable background-free signals through time-delayed signal measurements, a capability not achievable with organic dyes and QDs. Note that τ values of Eu^{3+} (x = 0.1 to 0.9) increased with respect to that of x = 1 whereas τ values of Tb^{3+} (x = 0.1 to 0.9) decreased with respect to that of x = 0. This is attributed to the energy transfer from Tb^{3+} to Eu^{3+} in $GdEu_xTb_{1-x}O_3$@PAA/PDA nanoparticles.[59–61] The energy transfer efficiency (η_{ET}) was estimated using the formula $\eta_{ET} = 1 - (\tau_x/\tau_0)$ in which x = 0.1 to 0.9. The estimated η_{ET} values were ~0.25, as provided in Table S6† and plotted in Fig. S6.† These appreciable η_{ET} values indicate an efficient energy transfer between nearby electronic energy levels of Tb^{3+} and Eu^{3+} in the nanoparticles.

Water proton spin relaxivities

The water proton spin relaxation times and map images were measured before and after the conjugation of PDA to the $GdEu_xTb_{1-x}O_3$@PAA nanoparticles. Four samples (*i.e.*, x = 0.1, 0.3, 0.5, and 0.9) were measured since Gd primarily affects water proton spin relaxation due to its very high 4f-electron spin (s = 7/2). Longitudinal (r_1) and transverse (r_2) water proton spin relaxivities were estimated from the slopes of inverse longitudinal (T_1) and transverse (T_2) water proton spin relaxation times plots *versus* (Eu + Gd + Tb) concentrations (Fig. 8a & b and Table 2). All r_1 and r_2 values were considerably higher than those (4–5 s^{-1} mM^{-1}) of commercial Gd(III)-chelates for T_1 MRI contrast agents.[10–12] R_1 and R_2 map images exhibited clear dose-dependent contrast enhancements (Fig. 8c & d), indicating the potential of $GdEu_xTb_{1-x}O_3$@PAA and $GdEu_xTb_{1-x}O_3$@PAA/PDA nanoparticles as superior T_1 MRI contrast agents compared to commercial Gd-chelates. These results are owing to a high density of Gd^{3+} (s = 7/2) ions per nanoparticle, combined with good colloidal stability of the nanoparticles. Given that r_2/r_1 ratios are small (<2), the $GdEu_xTb_{1-x}O_3$@PAA and $GdEu_xTb_{1-x}O_3$@PAA/PDA nanoparticles are better suited as T_1 MRI contrast agents rather than T_2 MRI contrast agents, similar to Gd(III)-chelates.[10–12] The water-attracting capacity of the nanoparticles, and consequently, their r_1 and r_2 values are affected by surface-grafting materials. As shown in Table 2, the r_1 and r_2 values of the $GdEu_xTb_{1-x}O_3$@PAA/PDA nanoparticles were lower than those of the $GdEu_xTb_{1-x}O_3$@PAA nanoparticles due to PDA being less hydrophilic than PAA, reducing the water-attracting capacity of the nanoparticles.

X-ray attenuation properties

The X-ray attenuation power increases with increasing atomic number (Z).[7,62,63] Considering that Eu (Z = 63), Gd (Z = 64), and Tb (Z = 65) have similar atomic numbers, two samples of $GdEu_xTb_{1-x}O_3$@PAA/PDA nanoparticles (x = 0 and 1) under-

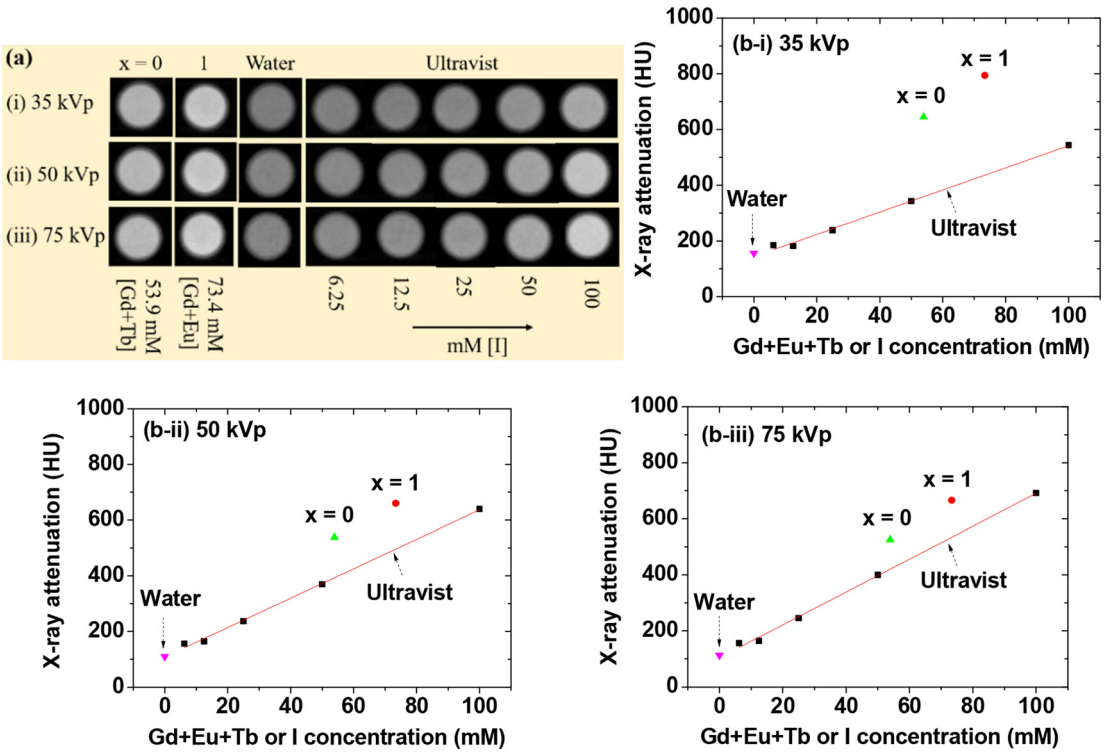

Fig. 9 (a) X-ray phantom images and (b) X-ray attenuation power plots of $GdEu_xTb_{1-x}O_3$@PAA/PDA nanoparticles in aqueous media for x = 0 (53.9 mM [Gd + Tb]) and x = 1 (73.4 mM [Eu + Gd]) at X-ray source voltages of (i) 35, (ii) 50, and (iii) 75 kVp. Water and Ultravist were used as references.

went X-ray phantom image measurements in aqueous media. Additionally, the Ultravist, a commercial iodine (Z = 53)-based CT contrast agent, was measured for comparison. As shown in Fig. 9a, the phantom images of the nanoparticle samples in aqueous media appeared brighter than those of Ultravist at similar atomic concentrations, indicating the superiority of $GdEu_xTb_{1-x}O_3$@PAA/PDA nanoparticles over iodine-based CT contrast agents. To demonstrate this quantitatively, the X-ray attenuation power was estimated using the phantom images in Hounsfield units (HU). The formula HU = 1000 $(\mu_{sample} - \mu_{water})/\mu_{water}$ was used, where μ represents the linear attenuation coefficient of the materials estimated from the phantom images. As illustrated in Fig. 9b, the samples exhibited higher X-ray attenuation power than Ultravist across X-ray source voltages of 35, 50, and 75 kVp. X-ray attenuation efficiencies (η; HU mM^{-1}) were ~10 HU mM^{-1} (Table 2), obtained by dividing observed X-ray attenuation power by atomic concentration (53.9 mM [Gd + Tb] and 73.4 mM [Eu + Gd]), ~2 times higher than those of Ultravist (4.0, 5.3, and 5.9 HU mM^{-1} at X-ray source voltages of 35, 50, and 75 kVp, respectively, estimated from the slopes in Fig. 9b-i, b-ii, & b-iii). These findings affirm the potential of $GdEu_xTb_{1-x}O_3$@PAA/PDA nanoparticles as CT contrast agents.

Cell viability

Given that all nanoparticle samples contain Eu, Gd, and Tb, two samples of $GdEu_xTb_{1-x}O_3$@PAA/PDA nanoparticles (x = 0 and 1) underwent MTT cell viability assay. Fig. 10 illustrates that cell viabilities for AML12 and Hek293 cells remained >90% at concentrations of up to 500 μM [Eu + Gd] and [Gd + Tb] for the two samples, indicating low cytotoxicity and thus the suitability of $GdEu_xTb_{1-x}O_3$@PAA/PDA nanoparticles for biomedical applications.

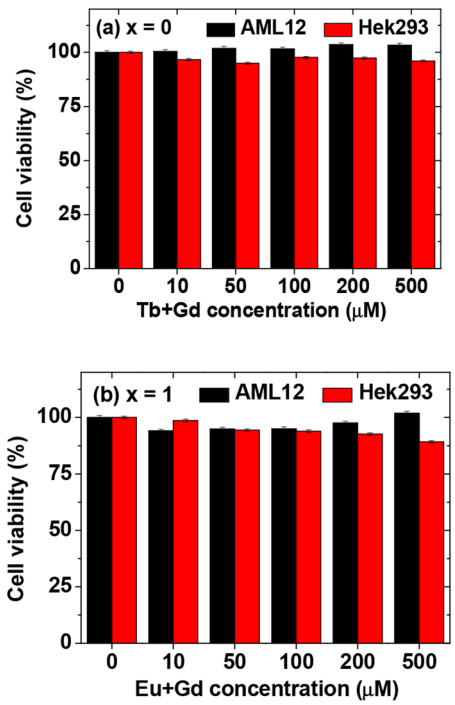

Fig. 10 MTT cell viability assay results for AML12 and Hek293 cells following a 48 h incubation with $GdEu_xTb_{1-x}O_3$@PAA/PDA nanoparticles [x = (a) 0 and (b) 1].

Conclusions

In summary, $GdEu_xTb_{1-x}O_3$@PAA/PDA nanoparticles (x = 0, 0.1, 0.3, 0.5, 0.7, 0.9, and 1) were synthesized with d_{avg} = ~2.0 nm. These nanoparticles exhibited colloidal stability (no precipitation in aqueous media for >1 year) and high cell viability (>90%). They demonstrated multiple exceptional properties within a single nanoparticle, suitable for various applications as follows:

1. The nanoparticles can transition between green (545 nm) and red (616 nm) by adjusting x, along with high absolute QYs (>30%) and long emission lifetimes (~1 ms) in aqueous media. This capability, facilitated by PDA conjugation as a photosensitizer, makes the nanoparticles suitable for optical imaging, noise-free signal detection, and colour display applications.

2. They exhibited r_1 values ~10 times higher than those of commercial Gd-chelate-based T_1 MRI contrast agents, with small r_2/r_1 ratios (<2), and η values ~2 times higher than those of commercial iodine-based CT contrast agents, making them suitable as both T_1 MRI and CT contrast agents.

Author contributions

D. Z., Y. L. and S. L. H. conceptualized the work and performed the preparation and characterization of the nanoparticles. T. T. and A. K. A. A. S analyzed data. H. L. measured water proton spin relaxivities and map images. D. A. and H. N. measured cell viability. J. A. P. and J.-u. Y. measured X-ray attenuation power. W.-S. C. measured PL spectra and QYs. Y. C. and G. H. L. drafted the manuscript. All authors have approved the final version of the manuscript.

Data availability

The raw data required to reproduce these findings will be made available upon request sent directly to the corresponding author.

Conflicts of interest

There are no conflicts to declare.

Acknowledgements

This work was supported by the Basic Science Research Program of the National Research Foundation (NRF) funded by the Korea government (Ministry of Science, and

Information and Communications Technology: MSIT) (Basic Research Laboratory, No. 2021R1A4A1029433).

References

1 J.-C. G. Bünzli, *Chem. Rev.*, 2010, **110**, 2729–2755.
2 S. V. Eliseeva and J.-C. G. Bünzli, *Chem. Soc. Rev.*, 2010, **39**, 189–227.
3 A. N. Kumar, D. M. Jnaneshwara, M. R. A. Kumar, N. Basavaraju, C. R. Ravikumar, H. C. A. Murthy, H. Nagabhushana, K. M. Girish, S. Ashwini and R. Naik, *Appl. Surf. Sci. Adv.*, 2020, **1**, 100026.
4 W. Xu, K. Kattel, J. Y. Park, Y. Chang, T. J. Kim and G. H. Lee, *Phys. Chem. Chem. Phys.*, 2012, **14**, 12687–12700.
5 H. Dong, S.-R. Du, X.-Y. Zheng, G.-M. Lyu, L.-D. Sun, L.-D. Li, P.-Z. Zhang, C. Zhang and C.-H. Yan, *Chem. Rev.*, 2015, **115**, 10725–10815.
6 A. F. Cotton and G. Wilkinson, *Advanced Inorganic Chemistry*, John-Wiley & Sons, New York, USA, 4th edn, 1980, pp. 981–985.
7 J. H. Hubbell and S. M. Seltzer, *Tables of X-ray Mass Attenuation Coefficients and Mass Energy-Absorption Coefficients from 1 keV to 20 MeV for elements Z = 1 to 92 and 48 Additional Substances of Dosimetric Interest*, NIST, Gaithersburg, MD, 1995, **https://physics.nist.gov/PhysRefData/XrayMassCoef/cover.html**.
8 T. Tegafaw, Y. Liu, S. L. Ho, S. Liu, M. Y. Ahmad, A. K. A. A. Saidi, D. Zhao, D. Ahn, H. Nam, W.-S. Chae, S.-W. Nam, Y. Chang and G. H. Lee, *Langmuir*, 2023, **39**, 15338–15342.
9 I. Milisavljevic, Y. Wu and E. Zych, *J. Lumin.*, 2020, **224**, 117243.
10 R. B. Lauffer, *Chem. Rev.*, 1987, **87**, 901–927.
11 P. Caravan, J. J. Ellison, T. J. McMurry and R. B. Lauffer, *Chem. Rev.*, 1999, **99**, 2293–2352.
12 J. Wahsner, E. M. Gale, A. Rodríguez-Rodríguez and P. Caravan, *Chem. Rev.*, 2019, **119**, 957–1057.
13 Z. Yi, Z. Luo, X. Qin, Q. Chen and X. Liu, *Acc. Chem. Res.*, 2020, **53**, 2692–2704.
14 Q. Zhang, S. O'Brien and J. Grimm, *Nanotheranostics*, 2022, **6**, 184–194.
15 P. G. Sammes and G. Yahioglu, *Nat. Prod. Rep.*, 1996, **13**, 1–28.
16 M. H. V. Werts, *Sci. Prog.*, 2005, **88**, 101–131.
17 L. Fu, Y. Wu and T. Fu, *J. Lumin.*, 2022, **245**, 118758.
18 A. Virender, A. Chauhan, G. Kumar, A. A. Singh, J. Solovev, J. Xiong, X. Liu and B. Mohan, *J. Rare Earths*, 2024, **42**, 16–27.
19 X. R. Wang, Y. P. Jiang, A. Tissot and C. Serre, *Coord. Chem. Rev.*, 2023, **497**, 215454.
20 H. Guan, M. Qi, L. Shi, W. Liu, L. Yang and W. Dou, *ACS Appl. Mater. Interfaces*, 2023, **15**, 18114–18124.
21 W. Fan, Y. Cheng, M. Feng, P. Liu, L. Wang, Y. Liu, Q. E. Cao and L. Y. Zheng, *ACS Appl. Mater. Interfaces*, 2023, **15**, 41977–41991.
22 M. Xiao and P. R. Selvin, *J. Am. Chem. Soc.*, 2001, **123**, 7067–7073.
23 S. Petoud, S. M. Cohen, J. C. G. Bünzli and K. N. Raymond, *J. Am. Chem. Soc.*, 2003, **125**, 13324–13325.
24 M. Latva, H. Takalo, V.-M. Mukkala, C. Matachescu, J. C. Rodríguez-Ubis and J. Kankare, *J. Lumin.*, 1997, **75**, 149–169.
25 M. Räsänen, J. Rosenberg, J. Lukkari, K. Haapakka, J. Kankare and H. Takalo, *J. Lumin.*, 2017, **187**, 471–478.
26 X.-F. Zhang, Y. Zhang and L. Liu, *J. Lumin.*, 2014, **145**, 448–453.
27 P. P. Pal and J. Manam, *Appl. Phys. A*, 2014, **116**, 213–223.
28 G. A. Sotiriou, M. Schneider and S. E. Pratsinis, *J. Phys. Chem. C*, 2011, **115**, 1084–1089.
29 G. V. L. Reddy, L. R. Moorthy, T. Chengaiah and B. C. Jamalaiah, *Ceram. Int.*, 2014, **40**, 3399–3410.
30 A. Podhorodecki, M. Banski, J. Misiewicz, M. Afzaal, P. O'Brien, D. Chad and X. Wang, *J. Mater. Chem.*, 2012, **22**, 5356–5361.
31 D. Qin and W. Tang, *RSC Adv.*, 2017, **7**, 2494–2502.
32 Y. Ding, Y. Wang, Y. Li, P. Cao and T. Ren, *Photochem. Photobiol. Sci.*, 2011, **10**, 543–547.
33 R. J. Aguado, B. O. Gomes, L. Durães and A. J. M. Valente, *Molecules*, 2023, **28**, 6164.
34 M. Massi and M. I. Ogden, *Materials*, 2017, **10**, 1369.
35 R. J. Batrice, A. K. Adcock, P. M. Cantos, J. A. Bertke and K. E. Knope, *Cryst. Growth Des.*, 2017, **17**, 4603–4612.
36 E. Bartolomé, J. Bartolomé, A. Arauzo, J. Luzón, R. Cases, S. Fuertes, V. Sicilia, A. I. Sánchez-Cano, J. Aporta, S. Melnic, D. Prodius and S. Shova, *J. Mater. Chem. C*, 2018, **6**, 5286–5299.
37 J. A. Dean, *Lange's Handbook of Chemistry*, McGraw-Hill, Inc., New York, USA, 14th edn, 1992, p. 1.290.
38 Eu_2O_3, 1977 JCPDS-International Centre for Diffraction Data, card no. 43-1008, the lattice constant = 10.859 Å.
39 Gd_2O_3, 1977 JCPDS-International Centre for Diffraction Data, card no. 43-1014, the lattice constant = 10.813 Å.
40 Tb_2O_3, 1977 JCPDS-International Centre for Diffraction Data, card no. 43-1032, the lattice constant = 10.730 Å.
41 W. Xu, B. A. Bony, C. R. Kim, J. S. Baeck and G. H. Lee, *Sci. Rep.*, 2013, **3**, 3210.
42 T. Tegafaw, W. Xu, M. W. Ahmad, J. S. Baeck, Y. Chang, J. E. Bae, K. S. Chae, T. J. Kim and G. H. Lee, *Nanotechnology*, 2015, **26**, 365102.
43 R. D. Shannon, *Acta Crystallogr., Sect. A: Cryst. Phys., Diffr., Theor. Gen. Crystallogr.*, 1976, **32**, 751–767.
44 K. Kattel, J. Y. Park, W. Xu, H. G. Kim, E. J. Lee, B. A. Bony, W. C. Heo, J. J. Lee, S. Jin, J. S. Baeck, Y. Chang, T. J. Kim, J. E. Bae, K. S. Chae and G. H. Lee, *ACS Appl. Mater. Interfaces*, 2011, **3**, 3325–3334.
45 G. B. Daecon and R. J. Philips, *Coord. Chem. Rev.*, 1980, **33**, 227–250.
46 C. B. Mendive, T. Bredow, M. A. Blesa and D. W. Bahnemann, *Phys. Chem. Chem. Phys.*, 2006, **8**, 3232–3247.
47 S. J. Hug and D. Bahnemann, *J. Electron Spectrosc. Relat. Phenom.*, 2006, **150**, 208–219.

48 R. G. Pearson, *J. Am. Chem. Soc.*, 1963, **85**, 3533–3539.
49 M. K. Corbierre, N. S. Cameron and R. B. Lennox, *Langmuir*, 2004, **20**, 2867–2873.
50 D. R. Lide, *CRC Handbook of Chemistry and Physics, Internet version 2005*, CRC Press, Boca Raton, FL, USA, 2005, pp. 4–57 (7.42 g cm^{-3}; Eu_2O_3), p. 4–58 (7.07 g cm^{-3}; Gd_2O_3), p. 4–89 (7.91 g cm^{-3}; Tb_2O_3): mol% averaged bulk density = 7.49 g cm^{-3} (x = 0), 7.47 g cm^{-3} (x = 0.1), 7.42 g cm^{-3} (x = 0.3), 7.37 g cm^{-3} (x = 0.5), 7.32 g cm^{-3} (x = 0.7), 7.27 g cm^{-3} (x = 0.9), and 7.25 g cm^{-3} (x = 1).
51 C.-H. Kim, I.-E. Kwon, C.-H. Park, Y.-J. Hwang, H.-S. Bae, B.-Y. Yu, C.-H. Pyun and G.-Y. Hong, *J. Alloys Compd.*, 2000, **311**, 33–39.
52 A. García-Murillo, C. Le Luyer, C. Dujardin, T. Martin, C. Garapon, C. Pédrini and J. Mugnier, *Nucl. Instrum. Methods Phys. Res., Sect. A*, 2002, **486**, 181–185.
53 I. P. Machado, V. C. Teixeira, C. C. S. Pedroso, H. F. Brito and L. C. V. Rodrigues, *J. Alloys Compd.*, 2019, **777**, 638–645.
54 A. D. Martinis, L. Montalto, L. Scalise, D. Rinaldi, P. Mengucci, C. Michail, G. Fountos, N. Martini, V. Koukou, I. Valais, A. Bakas, C. Fountzoula, I. Kandarakis and S. David, *Crystals*, 2022, **12**, 854.
55 T. R. Pisanic II, Y. Zhang and T. H. Wang, *Analyst*, 2014, **139**, 2968–2981.
56 M. Y. Berezin and S. Achilefu, *Chem. Rev.*, 2010, **110**, 2641–2684.
57 X.-F. Zhang, J. Zhang and L. Liu, *J. Fluoresc.*, 2014, **24**, 819–826.
58 R. Tang, H. Lee and S. Achilefu, *J. Am. Chem. Soc.*, 2012, **134**, 4545–4548.
59 J. Xu, C. He, L. Zeng, G. Li, C. Li, H. Lin, J. Liu, L. Zhou, J. Yang and J. Tang, *J. Lumin.*, 2024, **268**, 120398.
60 S. Li, N. Guo, Q. Liang, Y. Ding, H. Zhou, R. Ouyang and W. Lu, *Spectrochim. Acta, Part A*, 2018, **190**, 246–252.
61 A. N. Carneiro Neto, R. T. Moura Jr., A. Shyichuk, V. Paterlini, F. Piccinelli, M. Bettinelli and O. L. Malta, *J. Phys. Chem. C*, 2020, **124**, 10105–10116.
62 H. Lusic and M. W. Grinstaff, *Chem. Rev.*, 2013, **113**, 1641–1666.
63 S.-B. Yu and A. D. Watson, *Chem. Rev.*, 1999, **99**, 2353–2378.